ASME 2017 Summer Heat Transfer Conference
HT2017
July 9-14, 2017, Bellevue, Washington, USA

HT2017-5076

EFFECT OF PERFORATION SIZE TO PERFORATION SPACING ON HEAT TRANSFER IN LATERALLY PERFORATED-FINNED HEAT SINKS

Mohammad Reza Shaeri
Advanced Cooling Technologies, Inc.
Lancaster, PA, USA

Richard Bonner
Advanced Cooling Technologies, Inc.
Lancaster, PA, USA

ABSTRACT

Thermo-fluid characteristics of laterally perforated-finned heat sinks (LA-PFHSs) are investigated through experiments in laminar forced convection flows, in order to understand the key parameters affecting thermo-fluid transport phenomena and, in turn, parameters that play important roles to correlate heat transfer coefficients of LA-PFHSs. For this purpose, the Nusselt numbers of the LA-PFHSs are calculated using the well-accepted technique in the literature that was proposed to model Nusselt numbers of the slotted-finned heat sinks. Square cross sectional perforations at three different sizes are distributed along the length of the LA-PFHSs in inline configurations. Each perforation size is tested under five different porosities. The accuracy of the experiments are validated by comparing the pressure drops and Nusselt numbers of the imperforated heat sink against the correlated values obtained from the well-accepted correlations in the literature. Results indicate that the flow interactions over the perforations with each other are dominant mechanisms that affect transport phenomena in LA-PFHSs. The flow interactions with each other are proportional to the ratio of the perforation size to the solid distance between two-adjacent perforations. Therefore, this dimensionless geometrical parameter is found as the key parameter affecting thermo-fluid transport phenomena and, in turn, correlations to predict heat transfer coefficients of LA-PFHSs. At the end, suggestions are provided to develop physics-based correlations to predict heat transfer coefficients of LA-PFHSs through future research.

INTRODUCTION

Enhancing the heat transfer rate from air-cooled heat sinks is necessary due to the low thermal performances of air as the coolant. Interrupting the boundary layer in order to hinder its further growth over the surface is a potential technique to enhance the heat transfer rates, since a boundary layer acts like an insulation layer over the surface. Among different proposed techniques for the boundary layer interruption, perforated fins result in another advantage as lighter systems, due to perforations.

Generally, perforated fins are made by inserting perforations either along the length of the fins or on the lateral sides of the fins. A heat sink made from the former and latter groups of perforated fins is called a longitudinal perforated-finned heat sink (LO-PFHS), and a lateral perforated-finned heat sink (LA-PFHS), respectively. A LO-PFHS enhances the heat transfer rate through increasing the heat transfer area since individual perforations create separate channels along the length of the fins [1-6]. However, the mechanism of enhancement of heat transfer rate in a LA-PFHS relies on the boundary layer interruption, as such the boundary layer is frequently terminated and restarted before and after the perforations, respectively. Besides, since most commonly used industrial fins are thin with large aspect ratios, fabricating LO-PFHSs requires complicated and costly manufacturing techniques, while inserting perforations on the lateral surfaces of the fins can be performed through much simpler and more cost-efficient manufacturing techniques. As a result, LA-PFHSs are the subject of the present study.

Despite extensive research in thermal-fluid characteristics of solid-finned heat sinks (SFHSs, regular heat sinks with imperforated fins), research in LA-PFHSs is scarce, which has resulted in limited knowledge about the complex physics behind thermo-fluid transport phenomena in LA-PFHSs. Among few related studies, the computational works by Shaeri et al. [7, 8] were among the first research to investigate pressure drops, heat transfer, and individual component drag forces in LA-PFHSs. These studies were motivation for further related research in LA-PFHSs [9-12]. Recently, the authors performed experiments to investigate heat transfer and pressure drops in LA-PFHSs, and demonstrated the capability of LA-PFHSs to improve the laminar thermal performances without any penalty in the pumping power [13, 14]. Moreover, for the first time, local thermal resistances inside the channels of LA-PFHSs were

presented in [13]. Also, thermal-fluid characteristics of LA-PFHSs for a wider range of Reynolds numbers (laminar to turbulent) were investigated in the recent study by the authors [15].

Describing heat transfer coefficients of LA-PFHSs is beneficial in R&D efforts in order to design lightweight heat sinks to improve heat transfer characteristics. However, correlating heat transfer coefficients of LA-PFHSs has remained a challenge, due to a lack of knowledge about the complex physics behind transport phenomena in these cooling devices. Although Shaeri et al. [7, 8] proposed correlations to describe heat transfer coefficients of LA-PFHSs as functions of porosity and Reynolds number, these correlations are not physics-based and were developed by curve-fitting of the computational results. Frequent termination and restarting of the boundary layer, as well as the interactions of the flows over the perforations with each other, result in a complex physics that becomes more challenging by increasing the number of perforations, or by changing the configuration of perforations. In our recent study in [13], it was demonstrated that reporting heat transfer coefficients (h) of a LA-PFHS by inserting the open area (A) of the heat sink into $h = \frac{Q}{A\Delta T}$ would underestimate/overestimate heat transfer coefficients because of a monotonic change in the open area by increasing the porosity; while, through the experiments, it was shown that increasing the porosity beyond a threshold value at a given perforation size would deteriorate heat transfer [13]. An open area of a perforated fin represents the solid area of the lateral sides of the fin plus interior surfaces of the perforations. On the other hand, using the correlations that have been developed to predict heat transfer coefficients of SFHSs may not be accurate to describe heat transfer coefficients of LA-PFHSs due to different physics behind transport phenomena in SFHSs and LA-PFHSs, which mainly is because of frequent interruption of the boundary layer in LA-PFHSs. Therefore, such an uncertainty in accuracy of the correlations to predict the thermal performances of LA-PFHSs has hindered commercialization of these cooling systems, as such still SFHSs are the dominantly used heat sinks.

The present study is a supplement to our recent study in [13]. The main focus of the present study is understanding the key parameters that play important roles in both thermo-fluid transport phenomena in LA-PFHSs and correlations to predict heat transfer coefficients of LA-PFHSs. For this purpose, the experimental Nusselt numbers of LA-PFHSs are described through the well-accepted technique in the literature that was developed for predicting Nusselt numbers in slotted finned heat sinks. The experiments are performed by using three different perforation sizes and five porosities at each perforation size in laminar forced convection flows. The present study is the first experimental attempt to discuss the main parameters that affect correlations to predict Nusselt numbers by considering a wide range of perforation sizes and porosities. The findings from this study would be beneficial for future research to develop physics-based correlations to predict heat transfer coefficients of LA-PFHSs.

EXPERIMENT

The CAD model of the experimental setup, and the exploded view of the setup in this study are illustrated in Figures 1(a) and 1(b), respectively. Number 1 in Figure 1(b) pointes to the heat sink. A centrifugal blower (RG90-18/12N, ebm-papst Inc.) provided the airflow through a 91 cm long stainless steel duct with a rectangular cross section of 7.3 cm by 4.3 cm. The air velocities inside the duct were adjusted by regulating voltages of a 0-30 VDC power supply (CSI3005X5, Circuit Specialists, Inc.) that powered the blower. Two resistance temperature detector (RTD) probes (PR-26A-3-100-A-1/8-0600-M12-1, OMEGA Engineering, Inc.) at the entrance and exit of the heat sink measured the inlet and outlet air temperatures, respectively. The duct, blower, inlet, and outlet RTDs are numbered as 2, 3, 4, and 5, respectively, in Figure 1 (b). A differential pressure transducer (DPT) (PX653-01D5V, OMEGA Engineering, Inc.) measured the pressure drop across the duct. The high and low-pressure sensors of the DPT were located between the blower and the heat sink entrance (number 6 in Figure 1(b)), and at the exit of the duct (number 7 in Figure 1(b)), respectively. Since the pressure drop between the fan and the entrance of the heat sink, as well as that between the exit of heat sink and the duct exit was negligible, the DPT location upstream and downstream of the duct did not affect the measured pressure drop across the heat sink. The top surface of the duct was formed by placing a transparent polycarbonate cover on the duct flange. The duct was completely airtight by placing an adhesive neoprene rubber gasket between the flange and the polycarbonate cover, which was clamped in place between the cover and the flange. The rubber gasket and polycarbonate cover are numbered as 8, and 9, respectively, in Figure 1(b).

Figure 2(a) illustrates the CAD model of a LA-PFHS with two rows and six columns of perforations. Heat sinks were made of 6063-T5 aluminum alloy, and included 19 parallel channels (20 fins) with the fin thickness at 0.96 mm, and the channel length, height, and width at 203 mm, 22.86 mm, and 2.18 mm, respectively. The thickness of the heat sink base was at 2.54 mm. Perforations with square cross sections were fabricated on the lateral surfaces of the fins through the electrical discharge machining technique. Totally, 16 heat sinks were used in the present experiments. Table 1 summarizes the geometrical parameters of the heat sinks. The SFHS was used as the base for comparisons. Individual LA-PFHSs are distinguished from each other in Table 1 by two numbers, as the first number represents the porosity, and the second number inside the parenthesis as the perforation size in mm. The porosity is defined as the ratio of void volume of the fins due to perforations, to the volume of the solid fin (without perforation), as follows:

$$\phi = \frac{\text{void volume}}{\text{solid fin volume}} = \frac{N_P L_P^2}{HL} \quad (1)$$

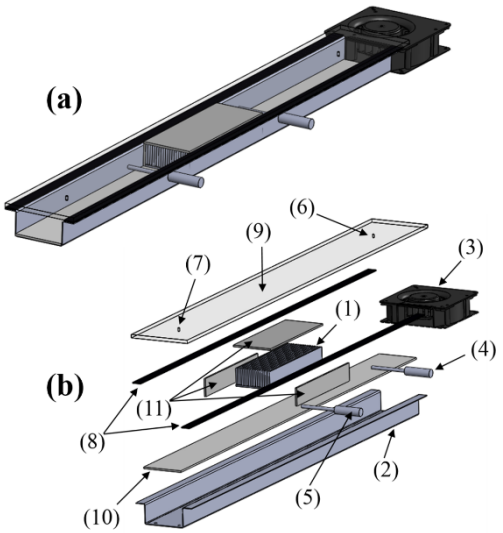

Figure 1. (a) The CAD model of the experimental setup, (b) the exploded view of the experimental setup.

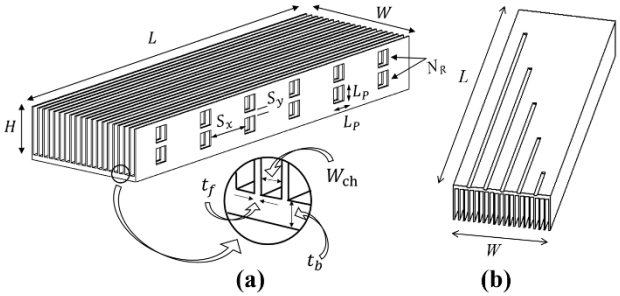

Figure 2. (a) The CAD model of a LA-PFHS with two rows and six columns of perforations, (b) bottom of the heat sinks.

As illustrated in Figure 2(b), five grooves at different distances from the inlet of the heat sink were machined on the heat sink base. Five T-type thermocouples (TJC36-CPSS-032G-12, OMEGA Engineering, Inc.) were placed in these grooves, and the spaces between the thermocouples and the grooves were filled with a bonding resin. An insulated flexible heater (KH-208/10-P, OMEGA Engineering, Inc.) was glued on the heat sink base, and provided a uniform heat load to the heat sink base. The heater was powered by a variable transformer (3PN116C, 0-140 V, 10 Amps, Superior Electric). The supplied voltage and current to the heater were measured using a multi-meter (FLUKE 117 TRUE RMS), and a clamp meter (FLUKE 376 TRUE RMS), respectively. In order to minimize the heat loss to the ambient, the floor of the duct, as well as the sides of the heat sinks, were covered by thermal insulation layers. The insulation layers at the floor of the duct, and around the heat sink are numbered as 10, and 11, respectively, in Figure 1(b). Signals from the thermocouples, RTDs, and differential pressure transducer were collected by a Keithley 2700 data acquisition system. The data was collected for three minutes of operation after reaching a steady state condition, which was considered to be reached when the changes in the temperatures obtained by individual embedded thermocouples and RTDs were below 0.2°C over a 10-minute period of operation. The experiments were proceeded by increasing the input blower voltage from 8 V to 14 V, by increments in 1 V. The experiments were conducted at two heat inputs of 50 W, and 100 W.

Table 1. Geometrical information of the perforations associated with the different heat sinks in this study.

Heat sink	N_P	L_P (mm)	S_x (mm)	S_y (mm)	N_R	ϕ
Solid	0	n/a	n/a	n/a	n/a	0
0.15 (5.08)	27	5.08	15.75	1.91	3	0.15
0.15 (7.62)	12	7.62	25.4	2.54	2	0.15
0.15 (15.24)	3	15.24	39.37	n/a	1	0.15
0.25 (5.08)	45	5.08	7.87	1.91	3	0.25
0.25 (7.62)	20	7.62	11.43	2.54	2	0.25
0.25 (15.24)	5	15.24	20.32	n/a	1	0.25
0.35 (5.08)	63	5.08	4.32	1.91	3	0.35
0.35 (7.62)	28	7.62	6.35	2.54	2	0.35
0.35 (15.24)	7	15.24	12.07	n/a	1	0.35
0.45 (5.08)	81	5.08	2.34	1.91	3	0.45
0.45 (7.62)	36	7.62	3.56	2.54	2	0.45
0.45 (15.24)	9	15.24	6.60	n/a	1	0.45
0.55 (5.08)	99	5.08	1.04	1.91	3	0.55
0.55 (7.62)	44	7.62	1.52	2.54	2	0.55
0.55 (15.24)	11	15.24	2.95	n/a	1	0.55

The airflow rates inside the duct $(\dot{V}_t)$ were determined by obtaining the actual operating point of the heat sink using the airflow bench (AMCA 210-99) at an individual blower voltage. The pumping power, as well as the volume flow rate, approach velocity, and Reynolds number inside an individual channel are calculated as follows:

$$P_p = \dot{V}_t \times \Delta P \tag{2}$$

$$\dot{V}_{\text{ch}} = \frac{\dot{V}_t}{N} \tag{3}$$

$$U = \frac{\dot{V}_{\text{ch}}}{W_{\text{ch}} H} \tag{4}$$

$$\text{Re} = \frac{\rho U D_h}{\mu} \tag{5}$$

The heat loss (Q_{loss}) from the heat sink to the ambient is calculated by subtracting the sensible absorbed heat by the air (Q_{conv}) from the electrical input heat (Q_{input}), as follows:

$$Q_{\text{loss}} = Q_{\text{input}} - Q_{\text{conv}} = I \times V - \left[\rho \dot{V}_t c_p (T_o - T_i)\right] \tag{6}$$

where I and V are the current and voltage, respectively, provided by the variable transformer, and c_p is the air specific heat. Since the heat loss in the present experiments ranged from 4.2-9.3%, it

is assumed that the whole input heat was absorbed by the heat sink; therefore, Q_{input} is used for the data reduction. For calculating the heat loss, the air properties were determined at the inlet temperature. However, for calculating other correlations, the air properties were determined at the film temperature as shown below:

$$T_{\text{film}} = \frac{T_{s,\text{avg}} + T_i}{2} \tag{7}$$

Using the assumption of one-dimensional heat diffusion in a distance d, which is the distance between the plane of the embedded thermocouples in the heat sink base and the fin base [16], the average temperature at the channel/fin base is calculated as follows:

$$T_{s,\text{avg}} = T_{b,\text{avg}} - \frac{Q_{\text{input}} d}{LWK_s} \tag{8}$$

and the average temperature at the base of the heat sink is calculated by taking an average of the local temperatures at the base of the heat sink, as shown below:

$$T_{b,\text{avg}} = \frac{\sum_{j=1}^{M} T_{b,j}}{M}, \quad M = 5 \tag{9}$$

The uncertainties of the instruments used in the present experiments were based on the information provided by their manufacturers, and are listed in Tables 2. The details about the uncertainties of all calculated values were provided in [13]; therefore, their explanations are omitted at the present study for the brevity.

Table 2. Uncertainty of the measured values.

RTD	$\pm(0.15 + 0.002t)$℃, which t is the temperature in ℃.
T-type thermocouples	$\pm$0.5℃.
Differential pressure transducer	0.3% of full scale.
Dimensions	$\pm 2.54 \times 10^{-2}$ mm.
Airflow bench	$\pm$2.0% of the measured flow rate.
Variable transformer	$\pm$2.0% of the voltage.

RESULTS

In the present experiments, the maximum Richardson number, as the ratio of the Grashof number to the square of the Reynolds number, was below 0.003 that indicates the forced convection as the dominant mode of heat transfer [13]. The accuracy of the experiment was validated by comparing the experimental pressure drops and Nusselt numbers of the SFHS against correlated values obtained by well-accepted correlations in the literature. The pressure drop across a heat sink is described as follows [17, 18]:

$$\Delta P = \frac{\rho U^2}{2}\left[K_c + 4x^+ f_{\text{app}}\text{Re} + K_e\right] \tag{10}$$

where

$$f_{\text{app}}\text{Re} = \left[\left(\frac{3.44}{\sqrt{x^+}}\right)^2 + (f\text{Re})^2\right]^{0.5} \tag{11}$$

$$x^+ = \frac{L}{D_h \text{Re}} \tag{12}$$

$$K_c = 0.42(1-\varepsilon) \tag{13}$$

$$K_e = (1-\varepsilon)^2 \tag{14}$$

The fraction of duct cross section that air passes through is calculated as follows:

$$\varepsilon = \frac{NW_{\text{ch}}H}{\text{duct cross sectional area}} \tag{15}$$

The Poiseuille number, $f\text{Re}$, for a laminar flow in a rectangular duct is described as follows [19]:

$$f\text{Re} = 24(1 - 1.3553\alpha + 1.9467\alpha^2 - 1.7012\alpha^3 + 0.9564\alpha^4 - 0.2537\alpha^5) \tag{16}$$

where α is the channel aspect ratio.

The correlation to predict Nusselt numbers in a plate-finned heat sink (SFHS) was proposed by Teertstra et al. [20] as shown below:

$$Nu_{\text{corr}} = \frac{\tanh\sqrt{2Nu_i \frac{KH^2}{K_s W_{\text{ch}} t}\left(\frac{t}{L}+1\right)}}{\sqrt{2Nu_i \frac{KH^2}{K_s W_{\text{ch}} t}\left(\frac{t}{L}+1\right)}} Nu_i \tag{17}$$

where

$$Nu_i = \left[\frac{1}{\left(\frac{\text{Re}_b^* \text{Pr}}{2}\right)^3} + \frac{1}{\left(0.664\sqrt{\text{Re}_b^* \text{Pr}^{1/3}}\sqrt{1+\frac{3.65}{\sqrt{\text{Re}_b^*}}}\right)^3}\right]^{-\frac{1}{3}} \tag{18}$$

$$\text{Re}_b^* = \frac{\rho U W_{\text{ch}}}{\mu} \times \frac{W_{\text{ch}}}{L} \tag{19}$$

In addition, based on the proposed definition in [20], the experimental Nusselt numbers in a channel of a plate-finned heat sink is calculated as follows:

$$Nu_{\exp} = \frac{\left(\frac{Q_{\text{input}}}{N}\right) W_{\text{ch}}}{K(2LH)\left(T_{s,\text{avg}} - T_i\right)} \tag{20}$$

Figures 3 and 4 illustrate the comparisons between the experimental and correlated pressure drops, and Nusselt numbers of SFHS, respectively. The maximum difference between experimental and correlated pressure drops, and that between the experimental and correlated Nusselt numbers are below 9.4%, and 8.0%, respectively, which indicates the good accuracy of the present experiments. In addition, the excellent agreements in Figure 3 represent the precise locations of the high and low pressure sensors of the differential pressure transducer in the air duct.

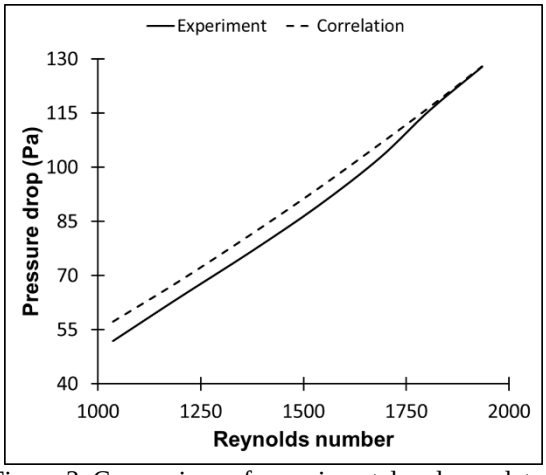

Figure 3. Comparison of experimental and correlated pressure drops in the SFHS.

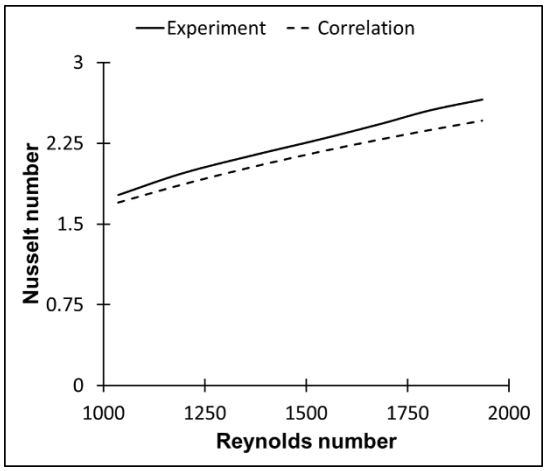

Figure 4. Comparison of experimental and correlated Nusselt numbers for the SFHS.

In order to understand the key parameters that affect average Nusselt numbers of LA-PFHSs, the proposed technique by Teertstra et al. [21] that was developed to model Nusselt numbers of slotted-finned heat sinks is used to describe the Nusselt numbers of LA-PFHSs in the present study. The reason of employing the developed model in [21] in the present study is a similar concept of frequent boundary layer interruptions in both slotted-finned heat sinks and LA-PFHSs due to slots and perforations, respectively.

Teertstra et al. leveraged their developed model to predict heat transfer coefficients of SFHS in [20], and proposed an analytical model in [21] to describe heat transfer coefficients of slotted-finned heat sinks in forced convection for the full range of Reynolds numbers from fully developed to laminar developing flow, and validated the accuracy of their model with experimental data. Teertstra et al. [21] defined lower and upper bounds for the thermal performance of the slotted-finned heat sink based on two limiting cases for the boundary layer growth. They assumed that the lower bound corresponds to not interrupting the boundary layer across the slotted fins, which results in thicker boundary layers and, in turn, lower heat transfer coefficients. On the other hand, the upper bound corresponds to when new thermal and hydrodynamic boundary layers are formed at each fin section, independent of any upstream effects. The lower bound is modeled by an equivalent channel with length corresponding to the combined length of all the fin sections, and the upper bound is modeled by considering a channel length corresponding to the length of a single fin section [21]. The equivalent lengths are substituted into two correlations, shown by Eqs (17) and (19).

By following the proposed technique in [21], the equivalent lengths for the lower bound and upper bound thermal performances of LA-PFHSs are as follows:

$$L_{LB} = L - \left(\frac{N_P}{N_R} \times L_P\right) \tag{21}$$

$$L_{UB} = S_x \tag{22}$$

where $\frac{N_P}{N_R}$ corresponds to the number of columns of perforations. However, while applying the proposed technique in [21] is appropriate in slotted-finned heat sinks, it faces some challenges in a LA-PFHS. Basically, a slotted-finned heat sink is made by cutting uniform cuts from the fin tip to the heat sink baseplate, on the lateral surfaces of the fins, as such the remaining fin sections are separated from each other and connected only by the heat sink baseplate [21]. Therefore, the height of a slotted fin is exactly the same as that of the solid fin. However, a LA-PFHS includes more interconnections between the solid sections on the lateral surface of a fin, which result in a complex fin height. Therefore, in the present study, the equivalent fin heights corresponding to lower and upper bounds of thermal performances are defined as shown below:

$$H_{LB} = H - (N_R \times L_P) \tag{23}$$

$$H_{UB} = S_y \tag{24}$$

As a result, four Nusselt numbers are calculated in the present study that are obtained by inserting the appropriate equivalent length and height in Eqs (17) and (19). These four Nusselt numbers are (i) $Nu_{L-LB,H-LB}$ that is obtained by using L_{LB} and H_{LB}, (ii) $Nu_{L-LB,H-UB}$ that is obtained by using L_{LB} and H_{UB}, (iii) $Nu_{L-UB,H-LB}$ that is obtained by using L_{UB} and H_{LB}, and (iv) $Nu_{L-UB,H-UB}$ that is obtained by using L_{UB} and H_{UB}. The upper and lower bound Nusselt numbers for the LA-PFHSs are obtained by averaging the Nusselt numbers associated with upper and lower bound fin heights at a given equivalent length, as follows:

$$Nu_{LB} = \frac{Nu_{L-LB,H-LB} + Nu_{L-LB,H-UB}}{2} \tag{25}$$

$$Nu_{UB} = \frac{Nu_{L-UB,H-LB} + Nu_{L-UB,H-UB}}{2} \tag{26}$$

In addition, the proposed correlation by Teertstra et al. [21] to calculate the experimental Nusselt numbers of slotted fins is used in the present study to calculate experimental Nusselt numbers of LA-PFHSs, as follows:

$$Nu_{\text{exp}} = \frac{\left(\frac{Q_{\text{input}}}{N}\right) W_{\text{ch}}}{K(2LH)(1-\phi)\left(T_{s,\text{avg}} - T_i\right)} \tag{27}$$

where Eq (27) describes the solid surface area on the lateral sides of two half perforated fins in an individual channel of a LA-PFHS. This equation is similar to Eq (20) for $\phi = 0$.

In the present study, the percentage of changes between the correlated and experimental Nusselt numbers for both upper bound and lower bound thermal performances are defined as follows:

$$\Omega_{UB} = \frac{Nu_{UB} - Nu_{\text{exp}}}{Nu_{\text{exp}}} \times 100 \tag{28}$$

$$\Omega_{LB} = \frac{Nu_{LB} - Nu_{\text{exp}}}{Nu_{\text{exp}}} \times 100 \tag{29}$$

Figures 5 to 7 illustrate Ω_{UB} for different porosities at given perforation sizes. First of all, the upper bound Nusselt number correlation for a slotted-finned heat sink results in significantly overestimated Nusselt numbers for all LA-PFHSs. This signifies that the boundary layer interruption is not the dominant mechanism that should be considered for developing correlations to predict heat transfer coefficients of LA-PFHSs. In addition, at a given perforation size, increasing the porosity leads to a monotonic enhancement of Ω_{UB}. This trend not only proves the aforementioned claim about the boundary layer interruption, but also indicates that the flow interactions over perforations with each other play a key role in transport phenomena in LA-PFHSs, because at a given perforation size, increasing the porosity corresponds to a decrease in S_x, which theoretically is associated with more frequent boundary layer interruptions and, in turn, larger upper bound Nusselt numbers, while the experimental Nusselt numbers are not enhanced. More flow interactions occur by increasing $\frac{L_P}{S_x}$ that is the ratio of the perforation size to the solid distance between two-adjacent perforations. The effects of flow interactions over the perforations were pointed out as one of the key parameters affecting heat transfer characteristics of LA-PFHSs in our recent study in [13], while they were not discussed in our previous study. The flow path lines over perforations were illustrated in the previous study by the author in [8] and are shown in Figure 8.

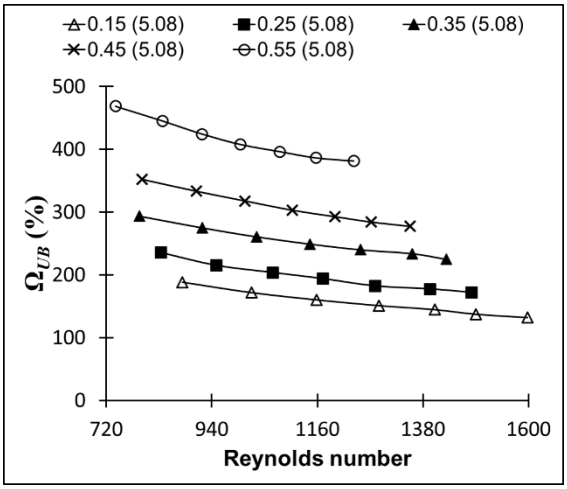

Figure 5. Percentage of changes between upper bound correlated Nusselt numbers and experimental Nusselt numbers for LA-PFHSs with perforation sizes at 5.08 mm.

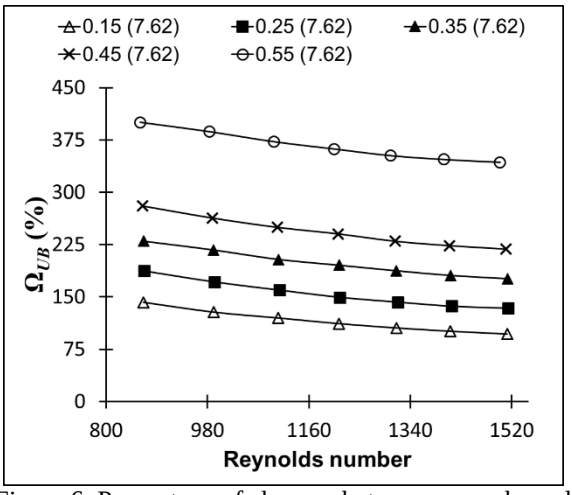

Figure 6. Percentage of changes between upper bound correlated Nusselt numbers and experimental Nusselt numbers for LA-PFHSs with perforation sizes at 7.62 mm.

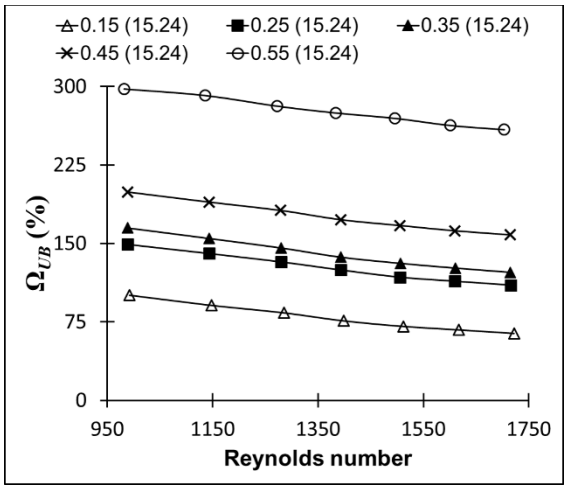

Figure 7. Percentage of changes between upper bound correlated Nusselt numbers and experimental Nusselt numbers for LA-PFHSs with perforation sizes at 15.24 mm.

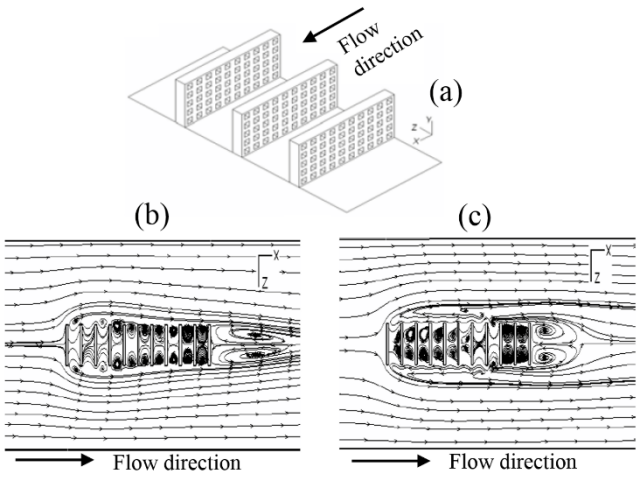

Figure 8. (a) a LA-PFHS with 50 perforations, (b) flow path lines at 30% height of the fins, (c) flow path lines at 70% height of the fins. Reprinted from Computational Thermal Sciences, Vol. 1, M. Yaghoubi, M.R. Shaeri, K. Jafarpur, Three-dimensional numerical laminar convection heat transfer around lateral perforated fins, pp. 323-340, 2009, with permission from Begell House, Inc.

Figures 9 to 11 illustrate the Ω_{LB} for different porosities at given perforation sizes. First of all, the overestimated Nusselt numbers for the LA-PFHSs with the largest porosity at all perforation sizes are again indications of the main effect of flow interactions over the perforations with each other due to a large value of $\frac{L_P}{S_x}$. On the other hand, the lower bound Nusselt number correlation underestimates the experimental Nusselt numbers for LA-PFHSs with both $L_P = 5.08$ mm and $L_P = 7.62$ mm at $\phi = 0.15 - 0.35$ through all Reynolds numbers, as well as the LA-PFHSs with $\phi = 0.45$ except at low Reynolds numbers. This trend is also observed throughout all Reynolds numbers for the LA-PFHS with $\phi = 0.15$, and for moderate to high Reynolds numbers for the LA-PFHS with $\phi = 0.25 - 0.45$ at the largest-size perforations with $L_P = 15.24$ mm. Since the lower bound correlated Nusselt numbers in [21] neglect the boundary layer interruption phenomenon, the negative values of Ω_{LB} for LA-PFHSs except at the largest porosity indicate that there is a threshold value of $\frac{L_P}{S_x}$, as such below that value both boundary layer interruptions and flow interactions are important to develop correlations for predicting the heat transfer coefficients of LA-PFHSs. However, beyond the threshold value of $\frac{L_P}{S_x}$, the flow interactions are the dominant mechanisms to explain transport phenomena in LA-PFHSs.

As a result, $\frac{L_P}{S_x}$ is found as one of the key parameters affecting thermo-fluid transport phenomena in LA-PFHSs and, in turn, correlations to predict heat transfer coefficients of LA-PFHSs. Further detailed research through flow visualizations is required to address the effects of flow structures over the perforations, as well as the flow interactions over the perforations with each other for a wide range of Reynolds numbers. Flow structures over perforations in low laminar flows would be different from those in the high Reynolds numbers. This can be observed by changing the values of both Ω_{UB} and Ω_{LB} for individual LA-PFHSs by increasing the Reynolds number. In addition, increasing the number of rows of perforations is another key parameter that would result in more flow interactions. While the present study covers the results related to inline perforation configurations, detailed research is required to investigate the transport phenomena in staggered configurations.

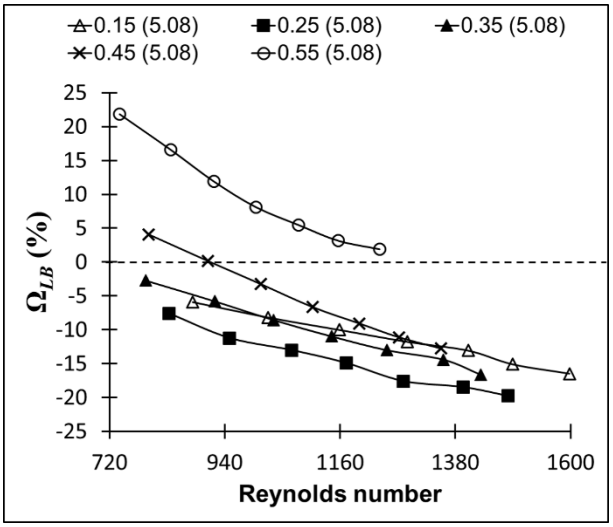

Figure 9. Percentage of changes between lower bound correlated Nusselt numbers and experimental Nusselt numbers for LA-PFHSs with perforation sizes at 5.08 mm.

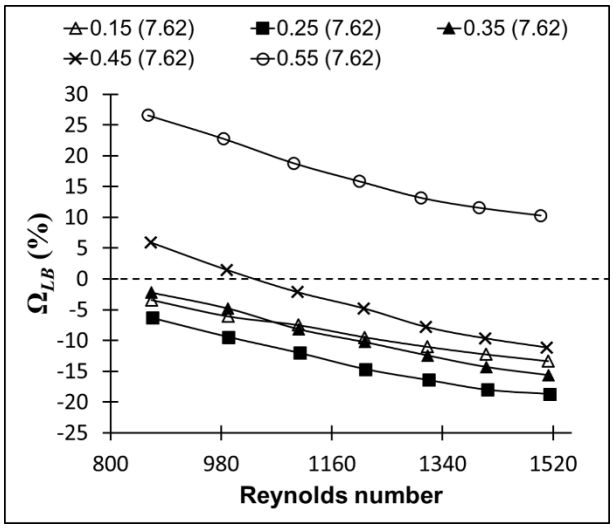

Figure 10. Percentage of changes between lower bound correlated Nusselt numbers and experimental Nusselt numbers for LA-PFHSs with perforation sizes at 7.62 mm.

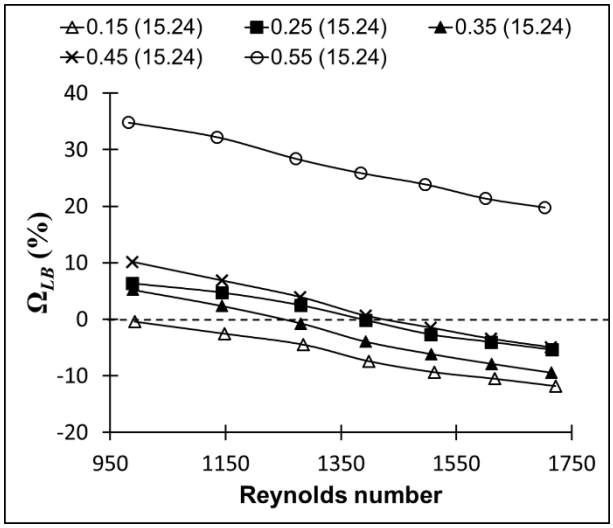

Figure 11. Percentage of changes between lower bound correlated Nusselt numbers and experimental Nusselt numbers for LA-PFHSs with perforation sizes at 15.24 mm.

CONCLUSION

Experiments were performed in laminar forced convection flows to investigate key parameters that affect thermo-fluid transport phenomena in LA-PFHSs, in order to provide an insight about developing physics-based correlations to predict heat transfer coefficients of LA-PFHSs. For this purpose, experimental Nusselt numbers of LA-PFHSs in this study were modeled by using a well-accepted technique in the literature that was proposed to model Nusselt numbers of slotted-finned heat sinks. Totally, 16 heat sinks were considered for conducting the experiments. In addition to a regular heat sink, three different perforation sizes, and five different porosities at each perforation size were considered. The accuracy of the experiments was validated by comparing the experimental pressure drops and Nusselt numbers against those values obtained from well-accepted correlations.

Results indicated that flow interactions over the perforations with each other are one of the key mechanisms affecting transport phenomena in LA-PFHSs. The dimensionless geometrical parameter of $\frac{L_P}{S_x}$ was found as a key parameter to interpret the transport phenomena in LA-PFHSs. It was found that there is a threshold value of $\frac{L_P}{S_x}$, as such beyond that value the flow interactions are the dominant mechanism, while both the boundary layer interruptions and flow interactions would be important for the values below the threshold $\frac{L_P}{S_x}$.

Suggestions were provided for further detailed research in order to develop physics-based correlations to describe heat transfer coefficients of LA-PFHSs.

NOMENCLATURE

D_h: Channel hydraulic diameter (m) $\left(\frac{2HW_{\text{ch}}}{H+W_{\text{ch}}}\right)$
H: Channel height (m)
K: Air thermal conductivity (W/K m)
K_s: Fin/heat sink thermal conductivity (W/K m)
L: Channel length (m)
L_P: Perforation length (m)
N: Number of channels
N_P: Number of perforations
N_R: Number of rows of perforations
Nu_{LB}: Lower bound correlated Nusselt numbers for LA-PFHSs
Nu_{UB}: Upper bound correlated Nusselt numbers for LA-PFHSs
P_p: Pumping power (W)
Q_{input}: Input electrical heat (W)
Re: Reynolds number
S_x: Distance between two adjacent perforations in a row (m)
S_y: Distance between two adjacent perforations in a column (m)
t_b: Thickness of heat sink base (m)
t_f: Fin thickness (m)
$T_{b,\text{avg}}$: Average temperature at the heat sink base (℃)
T_{film}: Film temperature (℃)
T_i: Inlet air temperature (℃)
T_o: Outlet air temperature (℃)
$T_{s,\text{avg}}$: Average temperature at the fin base (℃)
U: Air velocity inside the channel (m/s)
$\dot{V}_{\text{ch}}$: Volume flow rate inside the channel (m^3/s)
$\dot{V}_t$: Volume flow rate inside the duct (m^3/s)
W: Heat sink width (m)
W_{ch}: Channel width (m)

Greek symbols
ϕ: Porosity
Ω: Percentage in difference between correlated and experimental Nusselt numbers
ρ: Air density (kg/m^3)
μ: Dynamic viscosity (Pa.s)

Subscripts
LB: Lower bound
UB: Upper bound

ACKNOWLEDGEMENT

This material is based upon work supported by the National Science Foundation under Grant# IIP-1059286 to the American Society for Engineering Education.

The support extended by the Office of Science in the U.S. Department of Energy, award# DE-SC0011317 is gratefully acknowledged.

The authors are thankful to Ms. Abbey Gall for her support through the experiments.

REFERENCES

[1] M.R. Shaeri, M. Yaghoubi, Numerical analysis of turbulent convection heat transfer from an array of perforated fins, International Journal of Heat and Fluid Flow 30 (2009) 218-228.
[2] M.R. Shaeri, M. Yaghoubi, Thermal enhancement from heat sinks by using perforated fins, Energy Conversion and Management 50 (2009) 1264-1270.
[3] B. Sahin, A. Demir, Performance analysis of a heat exchanger having perforated square fins, Applied Thermal Engineering 28 (2008) 621-632.
[4] M.R. Shaeri, T-C. Jen, The effects of perforation sizes on laminar heat transfer characteristics of an array of perforated fins, Energy Conversion and Management 64 (2012) 328-334.
[5] M.R. Shaeri, T-C. Jen, Turbulent heat transfer analysis of a three-dimensional array of perforated fins due to changes in perforation sizes, Numerical Heat Transfer, Part A, 61 (2012) 807-822.
[6] Md. F. Ismail, M.O. Reza, M.A. Zobaer, M. Ali, Numerical investigation of turbulent heat convection from solid and longitudinally perforated rectangular fins, Procedia Engineering 56 (2013) 497-502.
[7] M.R. Shaeri, M. Yaghoubi, K. Jafarpur, Heat transfer analysis of lateral perforated fin heat sinks, Applied Energy 86 (2009) 2019-2029.
[8] M. Yaghoubi, M.R. Shaeri, K. Jafarpur, Three-dimensional numerical laminar convection heat transfer around lateral perforated fins, Computational Thermal Sciences 1 (2009) 323-340.
[9] Md. F. Ismail, M.N. Hasan, S.C. Saha, Numerical study of turbulent fluid flow and heat transfer in lateral perforated extended surfaces, Energy 64 (2014) 632-639.
[10] A. Willockx, Using the inverse heat conduction problem and thermography for the determination of local heat transfer coefficients and fin effectiveness for longitudinal fins, Doctoral dissertation, Ghent University, 2009.
[11] K.H. Dhanawade, V.K. Sunnapwar, H.S. Dhanawade, Optimization of design parameters for lateral circular perforated fin arrays under forced convection, Heat Transfer—Asian Research 45 (2016) 30-45.
[12] K.H. Dhanawade, H.S. Dhanawade, Enhancement of forced convection heat transfer from fin arrays with circular perforation, Frontiers in Automobile and Mechanical Engineering (2010) pp. 192-196, IEEE.
[13] M.R. Shaeri, R. Bonner, Laminar forced convection heat transfer from laterally perforated-finned heat sinks, Applied Thermal Engineering 116 (2017) 406-418.
[14] M.R. Shaeri, B. Richard, R. Bonner, Cooling performances of perforated-finned heat sinks, ASME 2016 Heat Transfer Summer Conference collocated with the ASME 2016 Fluids Engineering Division Summer Meeting and the ASME 2016 14th International Conference on Nanochannels, Microchannels, and Minichannels, Paper No. HT2016-7284, pp. V001T05A005, Washington, DC, USA, 2016.
[15] M.R. Shaeri, R. Bonner, H. Pearlman, Enhancing heat transfer rates across different flow regimes using perforated-finned heat sinks, Proceedings of the 2nd Thermal and Fluid Engineering Conference, April 2-5, 2017, Las Vegas, NV, USA.
[16] J. Lee, I. Mudawar, Two-phase flow in high-heat-flux micro-channel heat sink for refrigeration cooling applications: Part II—heat transfer characteristics, International Journal of Heat and Mass Transfer 48 (2005) 941-955.
[17] P. Canhoto, A.H. Reis, Optimization of forced convection heat sinks with pumping power requirements, International Journal of Heat and Mass Transfer 54 (2011) 1441-1447.
[18] S. Ndao, Y. Peles, M.K. Jensen, Multi-objective thermal design optimization and comparative analysis of electronics cooling technologies, International Journal of Heat and Mass Transfer 52 (2009) 4317-4326.
[19] M.E. Steinke, S.G. Kandlikar, Single-phase liquid friction factors in microchannels, International Journal of Thermal Sciences 45 (2006) 1073-1083.
[20] P. Teertstra, M.M. Yovanovich, J.R. Culham, Analytical forced convection modeling of plate fin heat sinks, Journal of Electronics Manufacturing 10 (2000) 253-261.
[21] P. Teertstra, J.R. Culham, M.M. Yovanovich, Analytical modeling of forced convection in slotted plate fin heat sinks, ASME-PUBLICATIONS-HTD 364 (1999) 3-12.